Solid State Ionics 353 (2020) 115369

Contents lists available at ScienceDirect

Solid State Ionics

journal homepage: www.elsevier.com/locate/ssi

Disagreements between space charge models and grain boundary impedance data in yttrium-substituted barium zirconate

Tarjei Bondevik[a,*], Jonathan M. Polfus[b], Truls Norby[a]

[a] Centre for Materials Science and Nanotechnology, University of Oslo, POB 1126 Blindern, NO-0318 Oslo, Norway
[b] SINTEF Industry, Sustainable Energy Technology, POB 124 Blindern, NO-0314 Oslo, Norway

A B S T R A C T

Although the space charge model is commonly used to explain the high grain boundary resistance in proton conducting yttrium-substituted $BaZrO_3$, it fails in its simplest forms with factors 10–40 to fit experimental data with respect to the characteristic frequency of the grain boundary impedance. We suggest modifications to the model, somewhat improving its fit. Including trapping effects of protons near yttrium substituents reduces the error only by factors less than 1.6. Increasing the width of the grain boundary core reduces the error with factors of 1.5–3. Discretizing the space charge layer, such that protons can only reside on specific, discrete sites, reduces the error with another factor of around 2. Considering reduced proton mobility in the GB by reducing its effective area may give a reduction in the fitting error of a factor of 2. Varying the dielectric constant in the GB does not affect the error considerably. Neither each single modification, nor their combined effect, can, however, account for the majority of the discrepancy between the space charge model and experimental data.

1. Introduction

Impedance spectroscopy consistently shows that proton conducting yttrium-substituted $BaZrO_3$ (BZY) grain boundaries (GBs) exhibit a lower conductivity than the bulk region [1–7]. As no secondary phases are observed at the GBs, the low conductivity is commonly attributed to an intrinsic space charge effect: positively charged defects segregate to the GB core, leading to a depletion of positive charge carriers in space charge layers (SCLs) adjacent to the core. This is in line with the results and conclusions also for other ceramic proton conductors, such as Y-substituted $BaCeO_3$ [8,9], alkaline-earth substituted $LaNbO_4$ [10], as well as a range of oxide ion conductors [11–15]. Moreover, similar space charge properties have been reported for BZY surfaces and heterointerfaces [16–18].

Space charge modelling has largely rationalized the electrical properties of BZY grain boundaries on a macroscopic scale [1,2,11,19–22]. Notably, the ratio between the GB and bulk conductivity ($\sigma_{gb}/\sigma_{\infty}$) decreases with increasing temperature [1,2]. Such GB conductivity would be characteristic of a space charge layer, where the charge carrier depletion becomes less prominent at higher temperatures. While this temperature dependence may be a result of reduced mobility in the GB core, two experimental observations point in the direction that space charge contribution, i.e., an effect of concentration rather than mobility, indeed is dominant. First, there is an inverse correlation between yttrium concentration and the SCL width [2]. According to the space charge model, higher yttrium concentration reduces the screening length in the SCL. Second, impedance spectroscopy shows an inverse correlation between applied bias and GB capacitance [3,7]. Such behavior agrees with a space charge description, and is difficult to explain if reduced mobility was the cause of the increased GB resistance – the GB capacitance should then have remained largely unchanged under applied bias [7]. Computationally, density functional theory calculations consistently show segregation of effectively positive point defects to the GB core [23–27]. Hence, there are strong arguments for SCLs being responsible for a significant part of the increased GB resistance in BZY. If this is the case, it should be possible to model the aggregated GB impedance with a bottom-up approach by summation of the impedances from individual SCLs, and fit such a model to experimental data.

In this work, we show that the characteristic frequency of the impedance predicted by the space charge model is not consistent with experimental data, with a mismatch larger than one order of magnitude. Impedance spectroscopy data from the present work and previous reports, as well as data from density functional theory calculations, are utilized in the analysis. We discuss modifications in the space charge model that may improve the fit. Specifically, we consider the effect of 1) proton trapping next to the yttrium dopant; 2) discretized SCL concentration profiles; 3) varying width of the GB core; 4) reduced mobility of the GB core; and 5) varying dielectric constant in the SCL.

* Corresponding author.
E-mail address: tarjeibo@gmail.com (T. Bondevik).

https://doi.org/10.1016/j.ssi.2020.115369
Received 17 October 2019; Received in revised form 12 April 2020; Accepted 20 May 2020
Available online 16 June 2020

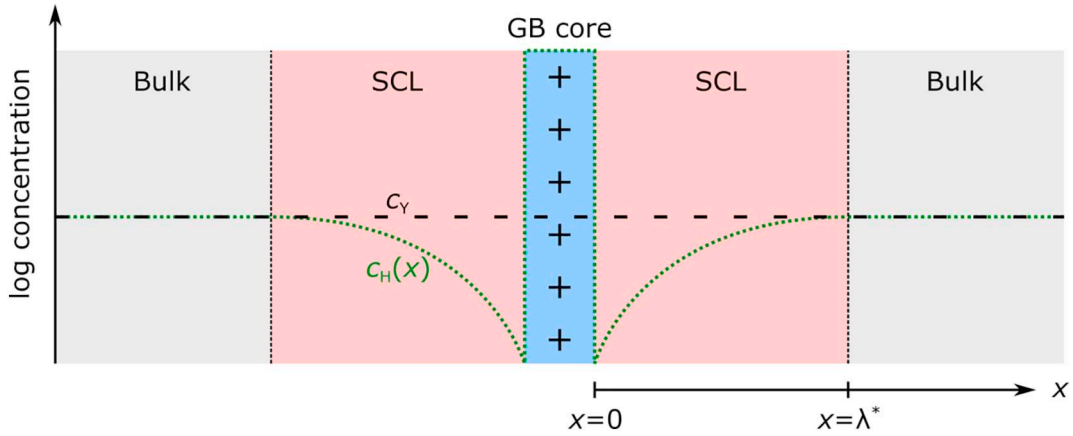

Fig. 1. Schematic of the GB region, with a positive GB core charge compensated by two adjacent SCLs. $x = \lambda^*$ marks the edge of the SCL region in the Mott-Schottky approximation.

2. Theoretical background

2.1. Derivation of the basic space charge model

For simplicity, we assume protons to be the dominant charge carrier BZY throughout the paper, although oxygen vacancies also contribute to the conductivity at higher temperatures and/or low water vapor partial pressures [28]. Furthermore, we assume constant proton mobility in the GB region. With these two assumptions, the resistivity becomes inversely proportional to the proton concentration.

Fig. 1 shows the three distinct regions considered in the basic space charge model. Due to structural distortions, point defects such as protons may be energetically more stable at the GB core, leading to defect segregation and, consequently, charge accumulation, at the core. While the GB core thereby acts as a trap for the excess protons, it can be expected to exhibit negligible resistance due to its narrow width and high proton concentration. To preserve the global charge neutrality of the material, the positive core is charge compensated by the depletion of protons in negatively charged SCLs adjacent to the core. The low proton concentrations gives a high effective resistivity (ρ_{gb}), defined as the average of the local resistivity, $\rho(x)$, in the SCL. The bulk regions adjacent to SCLs are charge neutral, with high, constant proton concentration, yielding high and constant proton conductivity (low resistivity ρ_∞).

The first step in the derivation is to find an expression for $\rho(x)$ in the SCL. Fig. 2 shows the relations between the quantities in the SCL model for a positively charged GB core. By assuming electrochemical equilibrium in the GB region, the local resistivity ratio in the SCL can be taken as [2].

$$\frac{\rho(x)}{\rho_\infty} = \frac{c_H}{c_H(x)} = \exp\left[\frac{e\Delta\phi(x)}{k_B T}\right], \tag{1}$$

where $\Delta\phi(x) \equiv \phi(x) - \phi_\infty$ is the electrostatic potential relative to the bulk potential, c_H the bulk proton concentration, $c_H(x)$ the SCL proton concentration, e the elementary charge, and $k_B T$ the thermal energy. An expression for $\Delta\phi(x)$ can be found by solving Poisson's equation. The one-dimensional Poisson's equation in the SCL is

$$\Delta\phi''(x) = -\frac{Q(x)}{\epsilon}, \tag{2}$$

where $Q(x)$ is the charge density in the SCL. Assuming constant yttrium concentration in the GB region (Mott-Schottky approximation) and that the SCL is fully depleted of protons yields

$$Q(x) = e(c_H(x) - c_Y(x)) \approx ec_Y. \tag{3}$$

With a constant charge in the SCL, Poisson's equation can be solved analytically. Applying the boundary conditions $\Delta\phi(\lambda^*) = \Delta\phi'(\lambda^*) = 0$

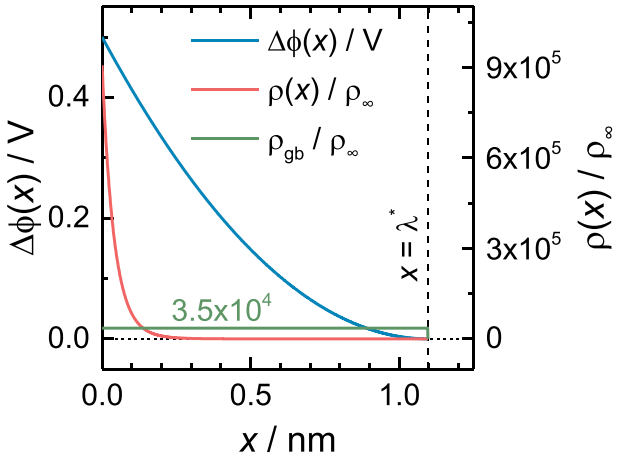

Fig. 2. The relations between the potential, the local resistivity and the effective resistivity in the SCL layer region. $x = \lambda^*$ marks the edge of the SCL region in the Mott-Schottky approximation. To obtain the above plot, Eq. (1) is solved, with $\Delta\phi(0) = 0.5$ V, $T = 423$ K, $\epsilon_r = 58$ and 20 mol% yttrium substitution.

gives its solution for $0 \le x \le \lambda^*$ [1],

$$\Delta\phi(x) = \Delta\phi(0)\left(\frac{x}{\lambda^*} - 1\right)^2, \tag{4}$$

with SCL length

$$\lambda^* = \left(\frac{2\epsilon\Delta\phi(0)}{ec_Y}\right)^{1/2}. \tag{5}$$

From the above equations, we observe that the local resistivity $\rho(x)$ in the SCL is a function of the potential at the GB core, $\Delta\phi(0)$. To determine $\Delta\phi(0)$, we assume that the entire GB resistance stems only from SCLs. Furthermore, we assume that all GBs in the material have equal resistance. With these assumptions, the basic space charge model can be fitted to the experimental data in two different ways.

2.2. Fitting impedance data based on intrinsic or geometric parameters

The high GB resistance of BZY depends on both intrinsic and geometric parameters, both of which can be extracted from impedance spectroscopy measurements. The characteristic frequency describes the intrinsic electrical properties of a material, and is found experimentally as the peak frequency of a Nyquist plot. The ratio between the GB and bulk characteristic frequency is

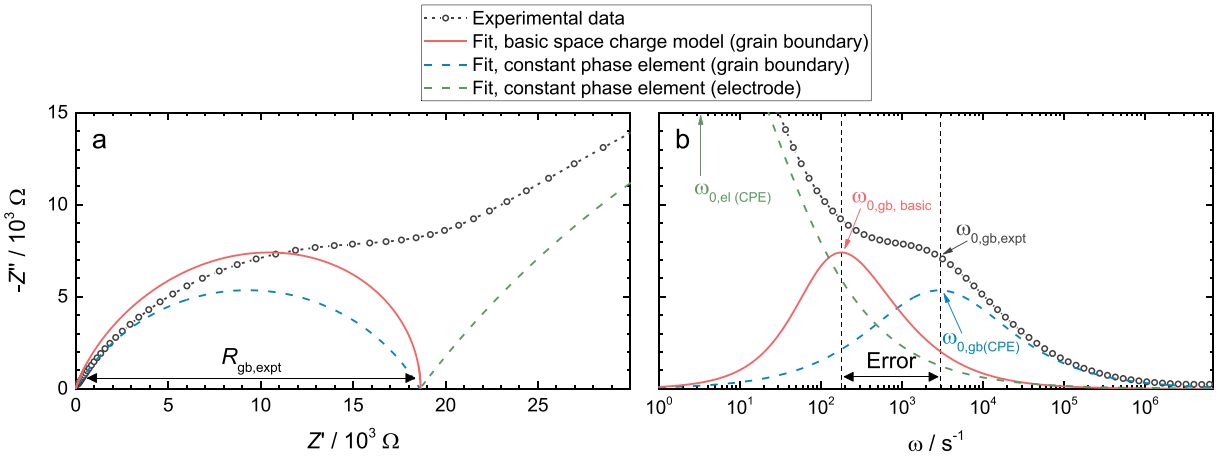

Fig. 3. Impedance spectroscopy results from the BZY15 sample at $T = 423$ K, comparing the basic space charge model with experimental results in a (a) Nyquist ($-Z''$ vs Z') plot, and (b) $-Z''$ vs ω plot, where CPE and el denotes constant phase element and electrode, respectively.

$$\frac{\omega_{0,\mathrm{gb}}}{\omega_{0,\infty}} = \frac{R_\infty C_\infty}{R_{\mathrm{gb}} C_{\mathrm{gb}}} = \frac{\rho_\infty \epsilon_\infty}{\rho_{\mathrm{gb}} \epsilon_{\mathrm{gb}}} = \frac{\rho_\infty}{\rho_{\mathrm{gb}}}, \tag{6}$$

where R is the resistance, C the capacitance, and ϵ the dielectric constant. In the last step, we assume constant permittivity in the GB region. The relevant geometric parameters appear in the expression for the GB resistance,

$$R_{\mathrm{gb}} = \rho_{\mathrm{gb}} \frac{\delta_{\mathrm{gb}}}{d_{\mathrm{grain}}} L, \tag{7}$$

where δ_{gb} is the width of the GB region, d_{grain} the average grain size and L the sample thickness. Here and throughout the paper the area of the sample and electrodes is set to unity for simplicity. An acceptable model describing the electrical response of a GB should satisfy both Eqs. (6) and (7) simultaneously.

To fit the experimental data to the basic space charge model, our first option is to fit with respect to intrinsic experimental parameters. The left hand side of Eq. (6), $\omega_{0,\mathrm{gb,expt}}/\omega_{0,\infty,\mathrm{expt}}$, is found experimentally, where expt denotes experimental parameters. To fit the basic space charge model to intrinsic parameters, we substitute the resistivity expression on the right hand side of Eq. (6) with the resistivity expression from the basic space charge model (Eq. (1)), yielding

$$\frac{\omega_{0,\mathrm{gb,expt}}}{\omega_{0,\infty,\mathrm{expt}}} = \left(\frac{1}{\lambda^*} \int_0^{\lambda^*} \exp\left[\frac{e\Delta\phi(x)}{k_{\mathrm{B}} T} \right] \mathrm{d}x \right)^{-1}, \tag{8}$$

where we have used that $\rho_{\mathrm{gb}} = \frac{1}{\lambda^*} \int_0^{\lambda^*} \rho(x)\mathrm{d}x$. The above equation can be solved numerically by approximating the integral to Riemann sums; its solution gives the modelled potential profile $\Delta\phi(x)$ in the SCL. With $\Delta\phi(x)$ known, the local SCL resistivity $\rho(x)$ can be found from Eq. (1). This method is sometimes referred to as the resistivity ratio method [29], used extensively in literature to extract GB potentials [1–3,12,13].

The second option is to fit the basic space charge model with respect to the experimental geometric parameters. First, the left hand side of Eq. (7), $R_{\mathrm{gb,expt}}$, is found experimentally. Second, we insert the resistivity expression from the basic space charge model (Eq. (1)) into the right hand side of Eq. (7), yielding

$$R_{\mathrm{gb,expt}} = \frac{2\rho_\infty L}{d_{\mathrm{grain}}} \cdot \int_0^{\lambda^*} \exp\left[\frac{e\Delta\phi(x)}{k_{\mathrm{B}} T} \right] \mathrm{d}x, \tag{9}$$

where the factor 2 is included to account for SCLs on both sides of the GB core. This equation is solved similarly as Eq. (8), yielding $\Delta\phi(x)$ and, subsequently, $\rho(x)$, in the SCL. To our knowledge, this method of extracting the GB potential has not been used in the literature. Eqs. (8) and (9) do not necessarily give the same, or even similar, potential profiles. As we will see, the subjective choice of fitting to either intrinsic or geometric parameters may greatly affect the modelled impedance.

Using $\rho(x)$ obtained either from Eqs. (8) or (9), the modelled impedance from a single space charge layer can be found as [30].

$$Z_{\mathrm{gb}} = \int_0^{\lambda^*} \frac{\rho(x)}{1 + j\omega\rho(x)\epsilon} \mathrm{d}x. \tag{10}$$

The above equation can be solved numerically by approximating the integral to Riemann sums. It is necessary to consider whether it is reasonable to calculate the SCL impedance from a continuous resistivity function, as done in Eq. (10). Our justification is based on our experimental data, laid out in Supplementary information A.

3. Disagreement between experimental data and the space charge model

3.1. Impedance comparison at a fixed temperature

First, we compare the modelled impedance with the experimental impedance at a fixed temperature. The experimental data was obtained from an impedance spectroscopy measurement on a BZY15 sample, acquired at $T = 423$ K. Fig. 3a shows a Nyquist plot, comparing the experimental data with the basic space charge model (subscript basic). A fit with a constant phase element [31] and a resistor in parallel (also shown) has been used to set $R_{\mathrm{gb,expt}}$, and geometric parameters (Eq. (9)) have been used to find $\rho(x)$. At first glance, the basic space charge model seems to fit experimental data fairly well, as both datasets yield similar, depressed semicircles. However, the frequency dependence of the modelled impedance (Fig. 3b) is off by more than one order of magnitude compared to the experimental data.

One possible source of error is that the exact experimental value $\omega_{0,\mathrm{gb,expt}}$ is hard to retrieve, due to the impedance contribution from the electrode at low frequencies. Note, however, that the frequency dependency of the impedance from the electrode is quite separated from the GB contribution (Fig. 3b), meaning that we can retrieve $\omega_{0,\mathrm{gb,expt}}$ fairly close to its true value. Critically, the uncertainty in $\omega_{0,\mathrm{gb,expt}}$ is much smaller than the difference between $\omega_{0,\mathrm{gb,expt}}$ and $\omega_{0,\mathrm{gb,basic}}$. Hence, we conclude that the basic space charge model does not reproduce the experimental GB impedance at this temperature.

3.2. Characteristic frequency comparison as a function of temperature

Fig. 4a compares the basic space charge model with experimental data as a function of temperature, where the relative fitting error $\omega_{0,\mathrm{gb,basic}}/\omega_{0,\mathrm{gb,expt}}$ is plotted. The basic space charge model was fitted

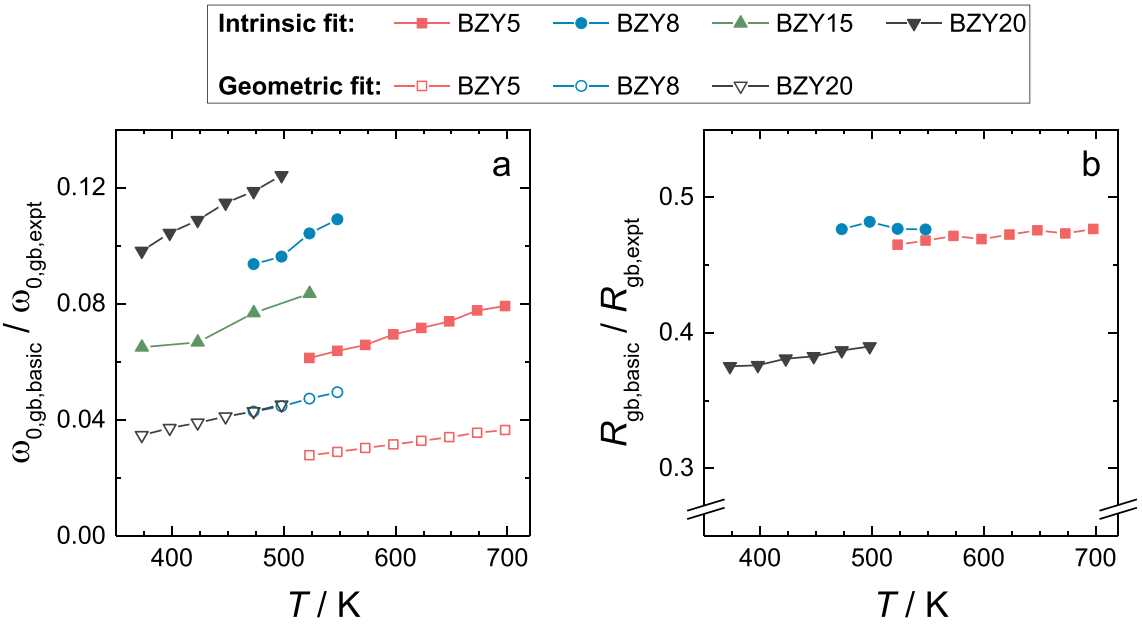

Fig. 4. Space charge model performance as a function of temperature and doping concentration for (a) $\omega_{0,gb,basic}/\omega_{0,gb,expt}$ ratio using intrinsic and geometric parameters, and (b) $R_{gb,basic}/R_{gb,expt}$ ratio using intrinsic parameters. Details about the samples are given in Table 1. The code used for the modelling is provided at GitHub: https://github.uio.no/tarjeibo/bondevik-phd-thesis

Table 1
Details about the samples used in the modelling. The sample name refers to the amount of yttrium doping in mol%.

Sample	ϵ_∞	d_{grain} [μm]	δ_{gb} [nm]	Reference
BZY5	66	0.24	12.4	Chen et al. [2]
BZY8	85	0.09	8.5	Chen et al. [2]
BZY20	58	0.40	4.9	Chen et al. [2]
BZY15	60	N/A	N/A	This work

with both approaches, i.e., based on intrinsic and geometric experimental parameters. An overview of the experimental data is given in Table 1.

When the SCL model is fitted to intrinsic data by Eq. (8), $\omega_{0,gb,basic}$ is too low by a factor of roughly 10–15. The value for $\omega_{0,gb,basic}$ was determined according to the following steps. First, $\Delta\phi(0)$ was obtained by fitting the basic space charge model to intrinsic parameters using Eq. (8). Second, $\rho(x)$ was obtained by inserting $\Delta\phi(0)$ into the expression for the local resistivity in Eq. (1). Third, $\rho(x)$ was inserted into the expression for the modelled impedance in Eq. (10); the impedance was modelled and the characteristic frequency extracted for comparison with the experimental value. The large error in the $\omega_{0,gb,basic}/\omega_{0,gb,expt}$ ratio can be understood by considering the effective resistivity ρ_{gb}. The local resistivity $\rho(x)$ is very different from ρ_{gb} in most of the space charge region (Fig. 2), with a high contribution from the innermost atomic layers. Noting that $\omega_0 \sim 1/\rho$, we should expect a low $\omega_{0,gb,basic}$, due to the dominance of the highly resistive innermost layers. Hence, fitting the effective resistivity ρ_{gb} to the basic space charge model by Eq. (8) will inevitably give a large error in the characteristic frequency.

Fig. 4b shows that the modelled GB resistance, $R_{gb,\ basic}$, is a factor of 2–3 lower than the experimental value, when fitting to intrinsic parameters. This error was calculated from two steps. First, the effective resistivity ρ_{gb} was obtained using Eq. (8). Second, ρ_{gb} was inserted into Eq. (7), and the modelled GB resistance was extracted for comparison with the experimental value. Fitting to intrinsic experimental parameters gives significant errors in the basic space charge model in both ratios, $\omega_{0,gb,basic}/\omega_{0,gb,expt}$ and $R_{gb,basic}/R_{gb,expt}$. The discrepancy holds for different doping levels and across a wide temperature range.

By fitting the basic space charge model to geometric parameters using Eq. (9) it is possible to model $R_{gb,basic}$ accurately, simply by adjusting $\Delta\phi(0)$ until the right hand side of Eq. (9) equals $R_{gb,expt}$. While this removes the error in $R_{gb,basic}$, it increases the error in $\omega_{0,gb,basic}$. Fig. 4a shows errors of factors 20–40 when geometric parameters are used for the fitting.

Hence, fitting to either intrinsic or geometric parameters yields space charge models that poorly match experimental data. In the following section, we discuss how the poor fit can be explained by limitations in the space charge model.

In the literature, fitting the model to intrinsic parameters with Eq. (8) is the common choice; in this work from now on, we will rather fit the model to geometric parameters through Eq. (9), for two reasons. First, getting a correct $R_{gb,basic}$ is then trivial, leaving $\omega_{0,\ gb,basic}$ as the single fitting parameter where the model should reproduce the experimental value. Second, one avoids using the somewhat arbitrarily defined effective resistivity. In the SCL, $\rho(x)$ varies with typically five orders of magnitude, so using the average ρ_{gb} for impedance calculations is questionable. By instead fitting experimental data to geometric parameters, this problem is bypassed.

4. Possible explanations for the disagreement

The basic space charge model presented until this point contains several simplifications and does not take into account several phenomena which may affect the GB impedance. We will now increase the complexity of the model by introducing additional physical aspects at the GB and different modelling approaches, and evaluate possible improvements in the fit to the experimental data.

4.1. Proton trapping

Experimental studies [32] and our DFT calculations in this work suggest that it is energetically favorable for protons to associate next to yttrium, described by the reaction (in Kröger-Vink notation)

$$(Y_{Zr} - O_O)' + OH_O^{\bullet} \leftrightarrow (Y_{Zr} - OH_O)^x + O_O^x, \tag{11}$$

with corresponding equilibrium constant

$$K_{(\mathrm{Acc-H})} = \frac{c_{(\mathrm{Y-H})}c_{\mathrm{O}}}{6c_{\mathrm{Y}}c_{\mathrm{H}}} = \exp(-\Delta E_{\mathrm{t}}/k_{\mathrm{B}}T), \quad (12)$$

where ΔE_{t} is the cluster binding energy, and c_{Y}, $c_{(\mathrm{Y-H})}$ and c_{O} are the bulk concentrations of unassociated yttrium, yttrium-proton clusters and oxide ions, respectively. The above bulk concentrations are found by imposing charge neutrality, $c_{\mathrm{Y}} = c_{\mathrm{H}}$, and mass balance, $A = c_{\mathrm{Y}} + c_{(\mathrm{Y-H})}$, where A is the acceptor doping level.

By considering proton trapping, the concentration of unassociated yttrium is reduced, leading to a less negative charge density in the SCL. This will affect the modelled SCL impedance, as one would need a wider SCL to compensate a given positive core charge. Most of the effect from proton trapping, however, vanishes due to the positive GB potential. With a positive potential, protons are strongly depleted, shifting the equilibrium (Eq. (11)) to the left-hand side. As the charge density can no longer be assumed to be constant in the SCL due to varying Y_{Zr}' concentration, Poisson's equation cannot be solved analytically. Poisson's equation was therefore solved numerically as a first order system of ordinary differential equations (ODEs), applying the two boundary conditions $\Delta\phi(0) = \Phi_0$ and $\Delta\phi'(\infty) = 0$, where Φ_0 is an initial guess of the GB core potential. Φ_0 was updated iteratively with small steps, until convergence was reached. The convergence criterion is the same as in Eq. (9), that is, when the modelled resistance equals the experimental GB resistance ($R_{\mathrm{gb,expt}}$). At each new Φ_0, an additional iterative loop was used to calculate $c_{\mathrm{Y}}(x)$, $c_{\mathrm{H}}(x)$ and $\Delta\phi(x)$ in the SCL, as these variables are interdependent through Eqs. (1), (2) and (12). Usually, five iterations were sufficient to achieve convergence of this additional loop. The trapping model is denoted trap, and basic* denotes a slightly modified basic space charge model, solved as a system of ODEs with varying proton concentration in the SCL. This modification is done to enable valid comparison with the trapping model, and has a small effect on the modelled characteristic frequency ($\omega_{0,\mathrm{gb,basic*}}/\omega_{0,\mathrm{gb,basic}} = 1.05$).

Fig. 5 compares the basic space charge model with two cases where trapping is considered, with cluster binding energies $\Delta E_{\mathrm{t}} = -0.14$ eV, found from our DFT calculations (dilute limit), and $\Delta E_{\mathrm{t}} = -0.30$ eV, found experimentally by Yamazaki et al. [32]. The comparison is done by fitting the models to experimental data from the BZY20 sample, at $T = 423$ K (see Table 1). Even though the bulk concentration of unassociated yttrium varies substantially as a function of cluster binding energy, they all approach the doping level of 20 mol% in the inner parts of SCL due to the strong positive potential in this region. Consequently, the proton concentrations in the inner parts of the SCLs are similar, and the modelled characteristic frequency remains largely unchanged. Using our computational binding energy $\Delta E_t = -0.14$ eV yields $\frac{\omega_{0,\mathrm{gb,trap}}}{\omega_{0,\mathrm{gb,basic*}}} = 1.04$, and the experimental value from Yamazaki [32] $\Delta E_t = -0.30$ eV yields $\frac{\omega_{0,\mathrm{gb,trap}}}{\omega_{0,\mathrm{gb,basic*}}} = 1.60$. Hence, considering trapping only slightly affects the modelled characteristic frequency. It gives a minor improvement by shifting the model somewhat closer to the experimental data, but not nearly enough to explain the discrepancy of factors 20–30 for the BZY20 sample.

4.2. Discretization of the space charge layer

In the basic space charge model, a potential profile is determined, and the proton concentration is evaluated as a continuous functional, infinitely close to the GB core. In a real material, protons are located at specific sites, and considering the proton concentration as a continuous function infinitely close to the GB core can be considered unphysical. In this modification of the space charge model, we discretize the SCL such that protons are only allowed to be located a specific distances $n \cdot d$ from the GB core, where d is the distance between the proton sites, and $n \in \left\{1, 2, ..., \mathrm{nint}\left(\frac{\lambda^*}{d}\right)\right\}$, with nint($x$) being a function returning the nearest integer to x. In such a model, the integral giving the impedance in Eq. (10) is replaced by a sum with n elements. To determine a plausible value for d, we note that the proton jump distance between oxygen sites in BZY is roughly 1.6 Å $\approx a_0/3$. Hence, a reasonable value for d can be around $a_0/3$, or perhaps slightly lower, as the proton may jump in directions not perpendicular to the GB plane.

By discretizing the SCL, the highly resistive region closest to the GB core in the basic space charge model is omitted from the calculation of the resistance. Thus, a larger $\Delta\phi(x)$ is needed to satisfy our convergence criteria in Eq. (9) that requires the modelled and experimental resistances to be equal. Fig. 6a shows the potential and the proton concentration when discretizing the SCL using $d = a_0/3$. The larger potential in the discretized model yields a lower proton concentration in most of the SCL. However, the minimum proton concentration is roughly 4 times larger in the discretized model compared to the basic model. Since $\omega_0 \propto \frac{1}{\rho} \propto c_{\mathrm{H}}(x)$ and the most resistive regions dominate the contribution to the characteristic frequency, the discretized model exhibits a higher characteristic frequency than the basic space charge model (Fig. 6b).

Fig. 7 compares the characteristic frequency of the discretized model with the basic space charge model as a function of temperature for various plausible values of d. For $d = a_0/3$, the $\omega_{0,\mathrm{gb,discrete}}/$

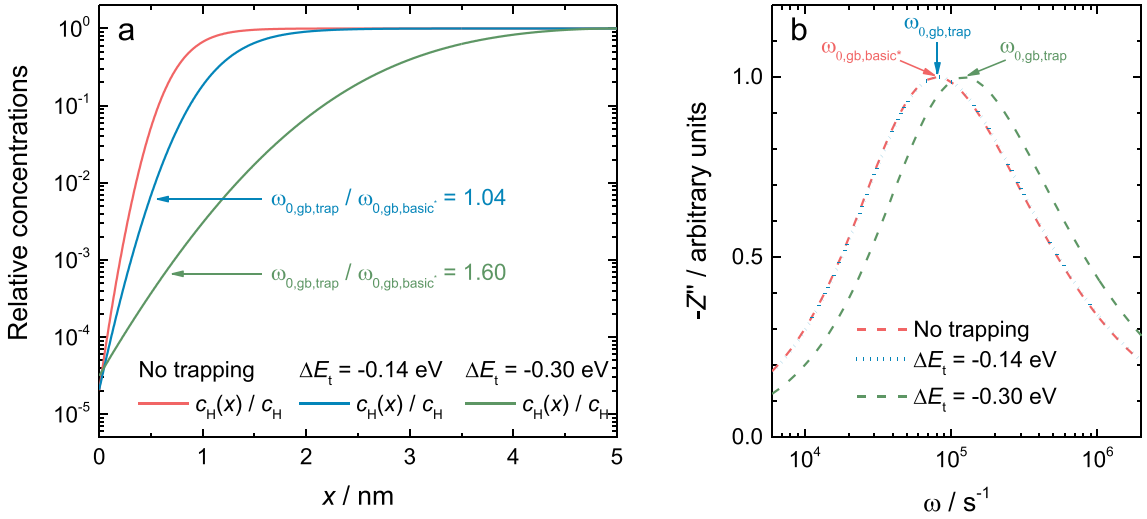

Fig. 5. The effect of trapping on found by fitting the model against experimental data from the BZY20 sample at $T = 423$ K, showing (a) proton concentration as a function of cluster binding energy and distance from the GB core, and (b) the imaginary impedance as a function of cluster binding energy and frequency. Note that the proton concentrations in (a) are given relative to their bulk values, hence they approach 1 at the end of the SCL.

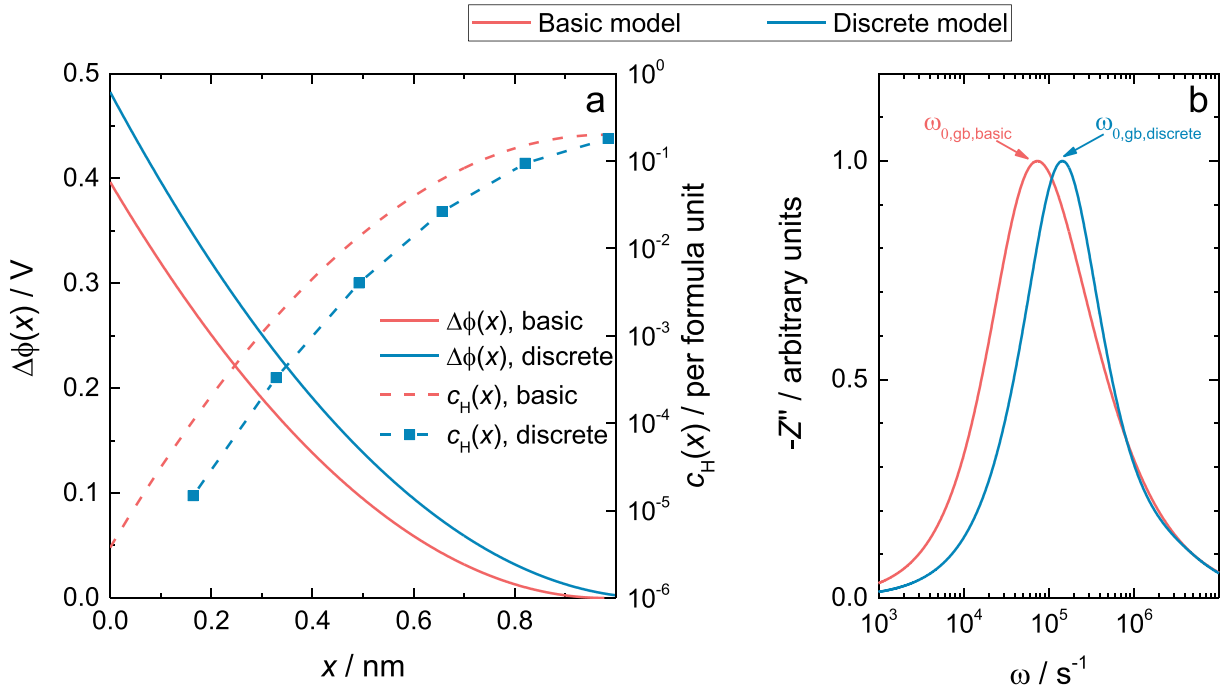

Fig. 6. The effect of discretizing the SCL, where $d = a_0/3$ have been used to fit the models to experimental data from the BZY20 sample at $T = 423$ K, showing (a) the potential and proton concentrations in the SCL, and (b) the imaginary impedance as a function of frequency.

$\omega_{0,gb,basic}$ ratio is around 2; for smaller d values, the effect diminishes as the model becomes closer to the continuous basic space charge model. Discretization also gives increased GB potentials, and the increase becomes larger for larger values of d. Although discretization does bring the model closer to experimental values, the effect is modest, and not nearly enough to explain the discrepancy of factors 20–30.

4.3. Widening the GB core

In the basic space charge model, the GB core and the SCL have been treated separately: the GB core is simply defined as a very thin, positively charged region, and the SCL reaches infinitely close to the core, with bulk structural properties all the way up to the core. In reality the interface may not be as abrupt, and the transition between bulk and core should most probably be more gradual. Our DFT calculated proton segregation energies in the (210)[001] grain boundary suggest that protons segregate towards multiple atomic planes in the GB region (see Fig. 8a), with a range of different segregation energies. This means that a segregation region wider than a single atomic plane, with *varying* segregation energy [24], should be considered in a space charge model. In this section, we will show how widening the GB core by applying different segregation energy functions affects the modelled characteristic frequency.

Our approach is to fit the segregation energy profile given in Fig. 8a as a Gaussian function with the Python scipy library [33]. This function, labelled Gaussian Fit A, can be written

$$\Delta E_{\mathrm{seg,A}}(x) = a_{\mathrm{A}} \exp\left[-\frac{(x-\mu_{\mathrm{A}})^2}{2\sigma_{\mathrm{A}}^2}\right]. \tag{13}$$

To study the GB width as a parameter, we introduce two additional Gaussian functions to represent the segregation energy. Gaussian Fit B has standard deviation $\sigma_{\mathrm{B}} = 2\sigma_{\mathrm{A}}$, expectation value $\mu_{\mathrm{B}} = \mu_{\mathrm{A}}$, with a_{B} set to satisfy

$$\int_{-\infty}^{\infty} \exp\left[-\frac{\Delta E_{\mathrm{seg,B}}(x)}{k_{\mathrm{B}}T}\right]\mathrm{d}x = \int_{-\infty}^{\infty} \exp\left[-\frac{\Delta E_{\mathrm{seg,A}}(x)}{k_{\mathrm{B}}T}\right]\mathrm{d}x. \tag{14}$$

Gaussian Fit C has standard deviation $\sigma_{\mathrm{C}} = 3\sigma_{\mathrm{A}}$, fitted to the same constraints as Fit B. All three functions are shown together with the segregation energy profile in Fig. 8a.

To assess the effect of the GB width, we applied the above segregation energy functions in a space charge model hereafter referred to as the Gaussian space charge model. The fitted segregation energy profiles were used to numerically solve Poisson's equation with the Jacobi method with the charge density

$$Q(x) = c_{\mathrm{H}}(x) - c_{\mathrm{A}} = c_{\mathrm{H},\infty}\cdot\exp\left[-\frac{\Delta E_{\mathrm{seg}}(x) + \Delta\phi(x)}{k_{\mathrm{B}}T}\right] - c_{\mathrm{A}} \tag{15}$$

used throughout the entire GB region. Note that the artificial distinction between the GB core and the SCL is no longer applied. Using the boundary conditions $\Delta\phi(-\infty) = \Delta\phi(\infty) = 0$, Eqs. (2) and (15) can be solved iteratively until convergence is reached when the system is charge neutral.

Fig. 8b shows the resulting potential profile from the three different segregation energy functions, modelled at $T = 423$ K. A larger standard deviation in the segregation energy function gives a wider potential profile, although the difference between Gaussian Fit B and C is small. Notably, Fig. 8c shows the concentration of protons throughout the GB region. Gaussian Fit A exhibits a small spread in the segregation energies. This gives a narrow charge profile, with the positively charged GB core being less than 0.2 nm wide, and a strongly depleted region next to the GB core. Gaussian Fit C has, in contrast, a wider segregation energy profile, yielding a wider but less depleted SCL.

To assess the effect of the three segregation energy profiles, we modelled the characteristic frequency ($\omega_{0,gb,wide}$) as a function of temperature, where subscript wide denotes the Gaussian space charge model. The space charge model with wide core due to a Gaussian segregation profile was compared with the basic space charge model, where $\Delta\phi(x)$ was found by demanding equal GB resistances in the two compared models, satisfying the condition

$$\int_{-\infty}^{\infty} \frac{c_{\mathrm{H},\infty}}{c_{\mathrm{H}}(x)}\mathrm{d}x = 2\cdot\int_{0}^{\lambda^*} \exp\left[\frac{e\Delta\phi(x)}{k_{\mathrm{B}}T}\right]\mathrm{d}x, \tag{16}$$

where the left- and right-hand sides represent $R_{\mathrm{gb,wide}}$ and $R_{\mathrm{gb,basic}}$,

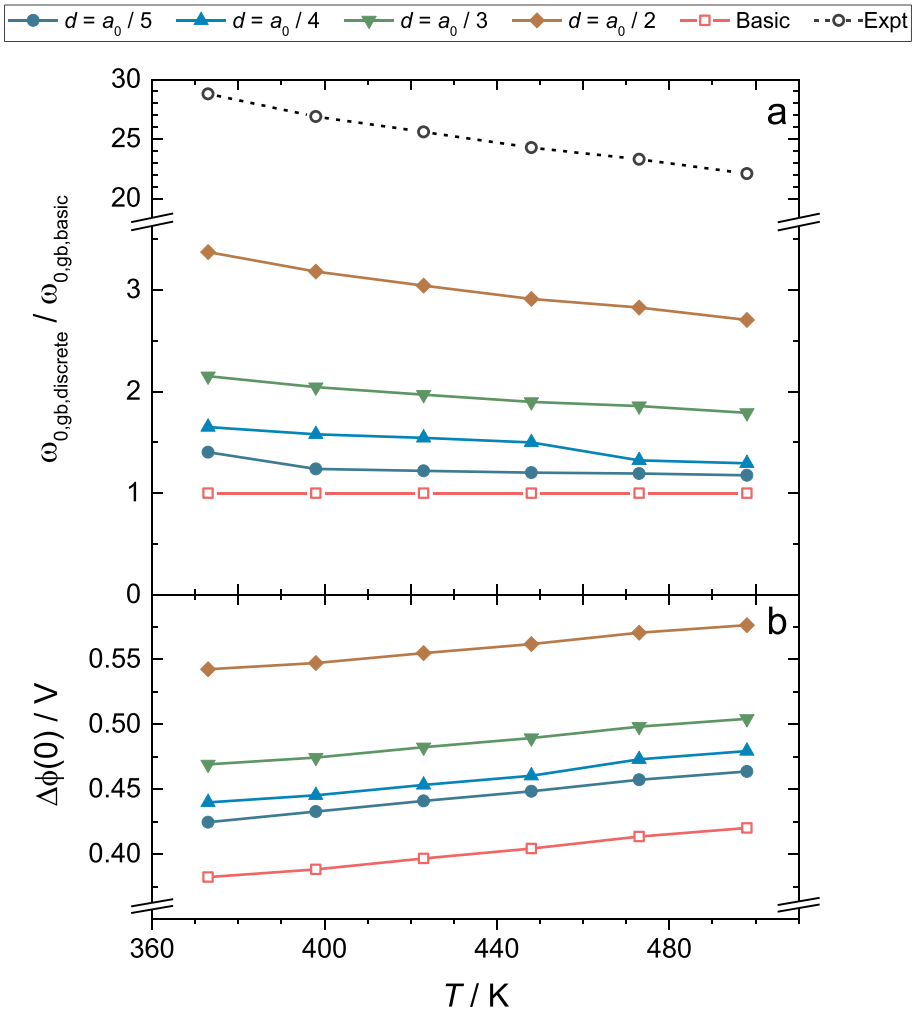

Fig. 7. The effect of the discretized model on the characteristic frequency (a) and the GB core potential (b) as a function of temperature, where the data was obtained by fitting the models to the BZY20 sample.

respectively. As shown in Fig. 9, the resulting $\omega_{0,gb,wide}/\omega_{0,gb,basic}$ ratio is in the range of 1.5–3, implying that widening the GB core improves the fit with experimental data. Furthermore, the match with experimental data improves with increasing width of the segregation energy function. Still, $\omega_{0,gb,wide}/\omega_{0,gb,basic}$ is fairly close to unity: widening the GB core brings the space charge model in the right direction, but is still far from explaining the discrepancy with experimental data.

Although considering a wider GB core probably more closely resembles the physical properties of a GB, it has several disadvantages. First, applying a Gaussian fit to the segregation energies requires – in the case of Fit B and C – subjective user input in setting the standard deviation parameter. Second, the model complexity is severely increased, limiting its availability.

One could consider widening the segregation energy profile even further than what we have done in Gaussian Fit C. This would have reduced the discrepancy between the space charge model and the experimental data. However, transmission electron microscopy imaging suggests that the GB core is around 1 nm wide [34], meaning that the region of non-zero segregation energy should be roughly the same. Hence, significantly wider segregation energy profiles than Gaussian Fit C are probably not physically justifiable.

Importantly, the widening of the GB core and the discretization of the SCL are not fully independent modifications. In both cases, the most strongly depleted region close to the core is omitted from the resistance calculation, and the effect on $\omega_{0,gb}$ is expectedly similar. Hence, if applied simultaneously, their combined effect on $\omega_{0,gb}$ is less than the product of the individual effects.

4.4. Reduced GB core proton mobility

Up to this point we have neglected any impedance contribution from the GB core. With the assumption of constant proton mobility μ_H in the entire GB region, the impedance in the GB core becomes negligible. This is seen from the expression for proton resistivity,

$$\rho = \frac{1}{ec_H\mu_H}, \tag{17}$$

where c_H is very large in the GB core, leading to a negligible GB core impedance. When looking more closely, however, assuming constant mobility in the GB region is a somewhat crude assumption.

The GB core is by definition a reduction in crystal symmetry, shown experimentally to be an important parameter for proton mobility in perovskites [28]. Furthermore, several computational studies show that structural distortions give significantly reduced proton mobility across the $BaZrO_3$ GB core [26,27]. The remaining question is whether the reduced mobility at the GB core can be visible in an impedance spectroscopy measurement. Even a very low GB mobility can be compensated by a large proton concentration or a very thin GB core, and hence have negligible contribution to the measured impedance.

In its simplest way, the reduced mobility can be described by splitting the GB into a conducting part with bulk mobility, and a blocking part with zero mobility. Considering the exponential

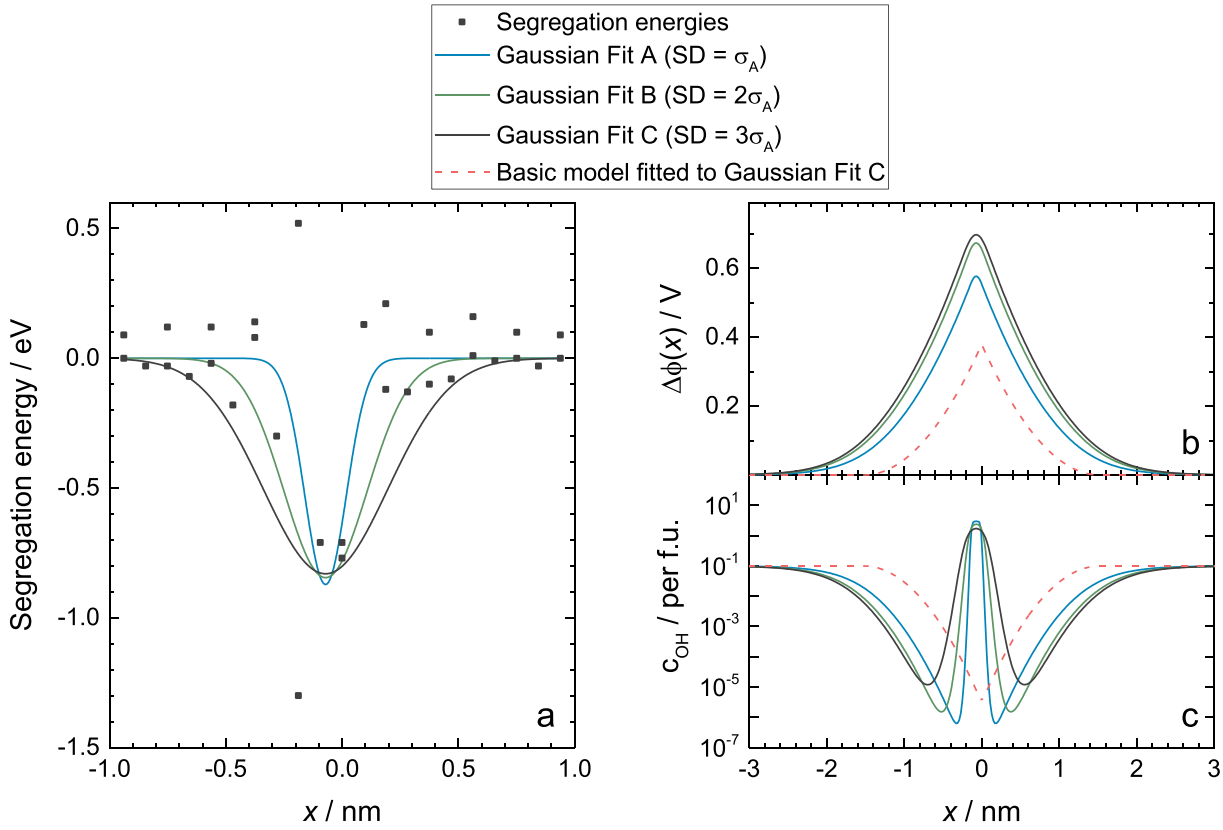

Fig. 8. Part (a) shows DFT calculated segregation energies, with three segregation energy functions, where SD in the legend indicates different standard deviations for the Gaussian functions. Parts (b) and (c) show the potential and proton concentration, respectively, for the different segregation energy functions, acquired at $T = 423$ K.

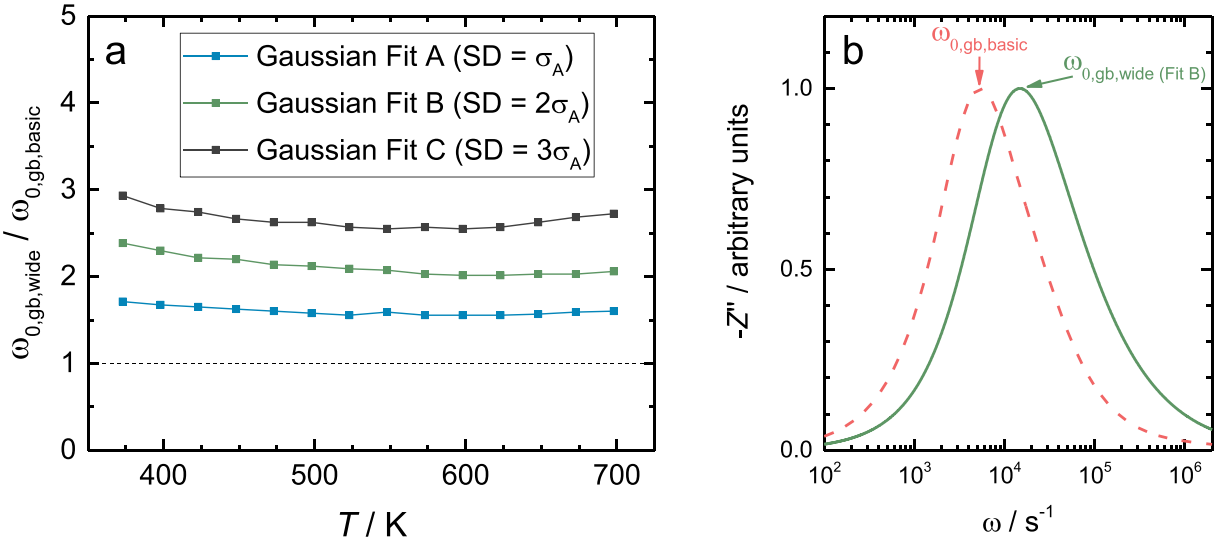

Fig. 9. Comparing the Gaussian space charge model with the basic space charge model, showing (a) GB characteristic frequencies, and (b) the imaginary impedance as a function of frequency, at $T = 423$ K.

dependence on migration barrier (see Eq. (19) below), a region of essentially zero mobility can be rationalized based on the large migration barriers (and trapping/segregation energies) obtained computationally. Letting $A_{\mathrm{eff,gb}}$ be the area of the conducting part, and A the total GB area, Eq. (9) can be updated to

$$R_{\mathrm{gb,expt}} = \frac{2\rho_{\infty}L}{d_{\mathrm{grain}}} \cdot \int_0^{\lambda^*} \exp\left[\frac{e\Delta\phi(x)}{k_{\mathrm{B}}T}\right] \mathrm{d}x \cdot \frac{A}{A_{\mathrm{eff,gb}}}. \tag{18}$$

A low conducting GB area $A_{\mathrm{eff,gb}}$ constraints the current and increases the GB resistance for a given resistivity. This means that a lower potential barrier $\Delta\phi(0)$ is needed to fit the experimental data, reducing the resistivity and thus increasing the characteristic frequency. Fig. 10a shows $\omega_{0,\mathrm{gb,area}}/\omega_{0,\mathrm{gb,basic}}$ as a function of $A_{\mathrm{eff,gb}}/A$, where subscript area denotes a space charge model with reduced effective area. As the area with zero mobility increases, $\omega_{0,\mathrm{gb,area}}$ approaches the experimentally measured value; at $A_{\mathrm{eff,gb}}/A = 0.5$, the error in the basic space

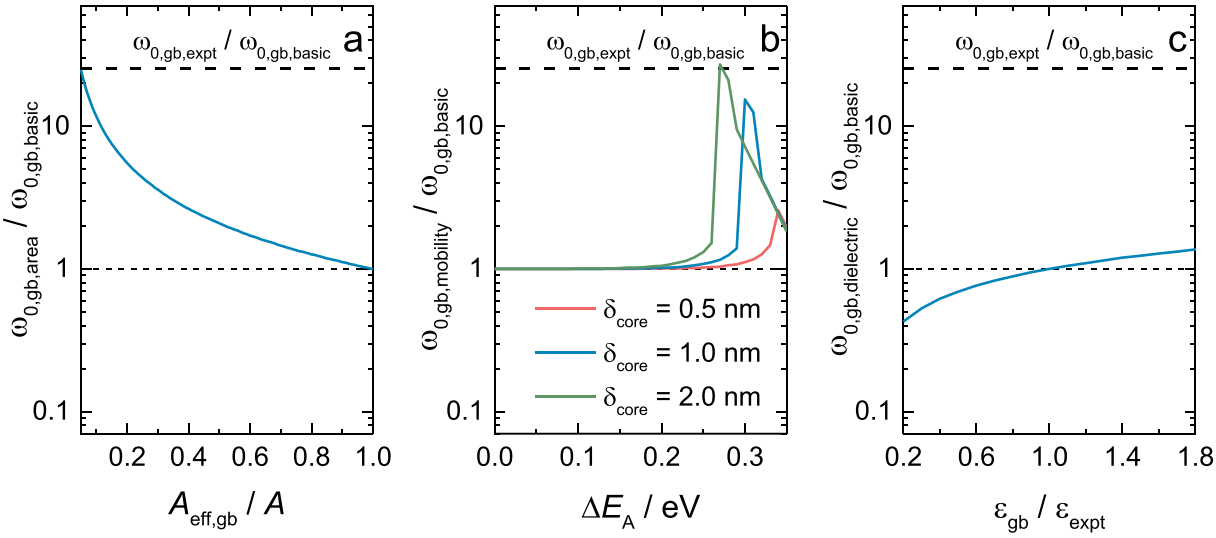

Fig. 10. The effect of (a) reduced effective GB area, (b) reduced GB proton mobility, and (c) varying dielectric constant on the modelled characteristic frequency and GB potential, on the BZY20 sample at $T = 423$ K.

charge model is reduced with a factor of 2. The exact value of $A_{\mathrm{eff,gb}}/A$ remains uncertain. In order to match the experimental data, however, $A_{\mathrm{eff,gb}}/A$ has to be less than 0.05, which seems unreasonably low.

A second approach is to rather treat the proton mobility explicitly in the impedance calculations. Let us define the ratio between the GB core and bulk mobility as

$$\frac{\mu_{\mathrm{core}}}{\mu_{\infty}} = \frac{\mu_{0,\mathrm{core}}\cdot\exp\left(-\frac{E_{A,\mathrm{core}}}{k_{\mathrm{B}}T}\right)}{\mu_{0,\infty}\cdot\exp\left(-\frac{E_{A,\infty}}{k_{\mathrm{B}}T}\right)} \approx \exp\left(-\frac{\Delta E_{\mathrm{A}}}{k_{\mathrm{B}}T}\right) \tag{19}$$

where μ_0 is a pre-exponential constant involving proton hopping distance and jump frequency, assumed to be equal in bulk and core for simplicity, and E_{A} is the activation energy, with $\Delta E_{\mathrm{A}} \equiv E_{\mathrm{A,core}} - E_{\mathrm{A},\infty}$. By considering the total GB resistance as a series connection between resistances from two SCLs and a GB core, Eq. (9) becomes

$$R_{\mathrm{gb,expt}} = \frac{2\rho_{\infty}L}{d_{\mathrm{grain}}}\cdot\int_0^{\lambda^*}\exp\left[\frac{e\Delta\phi(x)}{k_{\mathrm{B}}T}\right]\mathrm{d}x + \frac{\rho_{\infty}\delta_{\mathrm{core}}^2}{2\lambda^* + \delta_{\mathrm{core}}}\cdot\exp\left(\frac{\Delta E_{\mathrm{A}}}{k_{\mathrm{B}}T}\right). \tag{20}$$

A derivation of the second term in the above expression shown in Supplementary information B. Applying the expression yields the characteristic frequency as a function of ΔE_{A} (Fig. 10b), where subscript mobility denotes a space charge model with reduced proton mobility for three different GB core widths. The discontinuity in the plot occurs because the core contributes to a second semicircle in the Nyquist impedance plot. With increasing activation energy, the core semicircle starts to dominate at some threshold, leading to a discontinuous shift in the peak frequency ω_0. At activation energies above this threshold we no longer have a space charge model, as the total resistance is completely dominated by the GB core resistance, with $\Delta\phi(0) = 0$ (the second term in the right hand side of Eq. (20) becomes larger than $R_{\mathrm{gb,expt}}$, yielding $\Delta\phi(0) = 0$). Hence, we can only consider activation energies below that threshold within the framework of a space charge model. With that, reducing the proton mobility only gives a minor improvement (up to a factor of 1.5) on the modelled characteristic frequency ratio.

One possible way to solve this discontinuity problem could be to add inhomogeneity into the model, allowing different GB potentials within the same sample. This would lead to a smearing of the Nyquist plot, and possibly remove the discontinuity. However, introducing such inhomogeneities is beyond the scope of this the present work, and comes with its own problems, as it requires using even more fitting parameters. Furthermore, it is reasonable to assume that the main conclusion – that the modelled ω_0 becomes too small because of the highly resistive inner parts of the SCLs – will remain in such a model.

4.5. Dielectric constant

Strong lattice distortions close to the GB core is a good argument for questioning the usual assumption of $\epsilon_{\mathrm{gb}} = \epsilon_{\mathrm{bulk}}$. Fig. 10c shows $\omega_{0,\mathrm{gb,dielectric}}/\omega_{0,\mathrm{basic}}$ as a function of dielectric constant in the GB region, where subscript dielectric refers to this model, where the dielectric constant in the space charge layer, ϵ_{gb}, is varied relative to its bulk value. Even with significant changes in ϵ_{gb}, the modelled $\omega_{0,\mathrm{gb,dielectric}}$ remains largely unchanged, far from the experimental value. Hence, any deviation from the $\epsilon_{\mathrm{gb}} = \epsilon_{\mathrm{bulk}}$ assumption is not expected to explain much of the discrepancy between the basic space charge model and experimental data.

4.6. Gouy-Chapman approximation

Finally, we will briefly discuss the effect of the Gouy-Chapman approximation, where the yttrium dopants are considered mobile. With a positively charged GB core, negatively charged yttrium will accumulate according to the SCL potential profile. It may be noted that a frozen-in Y-profile may be more reasonable to consider for lower temperatures. The Gouy-Chapman approximation gives a sharper potential profile close to the GB core (Supplementary information C). Consequently, the depletion of protons close to the core increases, which leads to a reduction in the modelled characteristic frequency, and an increase in the error compared to the basic space charge model of up to a factor of 2.

Yttrium segregation towards the GB core may lead to reduced proton mobility due to trapping effects, and may therefore affect the characteristic frequency in the impedance data. The role of decreased proton mobility in the SCL may be considered similar to widening of the core and reduced core mobility, as covered in Sections 4.3 and 4.4.

5. Summary and conclusions

There is a large disagreement between the basic space charge model and experimental data. Specifically, the characteristic frequency of the basic space charge model deviates from experimental data with a factor of 10–40, due to the dominant contributions from the highly resistive innermost atomic layers closest to the GB core in the space charge model. This implies that the basic space charge model is not able to

correctly describe the impedance of a GB.

Even when we introduce additional free parameters and conduct a targeted effort to improve the fit of the space charge model, we end up with only minor improvements. Including proton trapping reduces the fitting error of $\omega_{0,\ gb}$ by a factor of 1–1.6. The effect of trapping is modest because the cluster concentration is low in the SCL. Widening the GB core reduces the fitting error of $\omega_{0,gb}$ by a factor of 1.5–3. Discretizing the SCL by only allowing the protons to be located at specific sites reduces the fitting error of $\omega_{0,gb}$ by a factor of around 2. Considering lower GB core mobility by reducing the effective area of the GB, reduces the fitting error of $\omega_{0,gb}$ by a factor of around 2 if $A_{eff,gb}/A = 0.5$; an appreciable fit was obtain only for a miniscule effective area of $A_{eff,gb}/A = 0.05$. Explicitly considering lower GB core mobility in the impedance calculations gives a negligible reduction in fitting error. Finally, setting $\epsilon_{gb} \neq \epsilon_{bulk}$ has a negligible effect on the modelled $\omega_{0,gb}$.

Other modifications to the space charge model not included in this work may, possibly, explain parts of the remaining discrepancy. One option is to apply so-called Poisson-Cahn theory that includes parametrizations of defect-defect interactions when solving Poisson's equation [35,36]. Another possibility could be to include current constraints on the atomic scale into the model. Since the GB core is highly asymmetric, some proton migration paths are likely to have very low mobility, which will lead to current constraints in the proximity of the GB core. Previously, current constraint due to resistive GBs has been modelled on the microscopic scale [37–39], and a similar approach on the atomic scale may be fruitful.

By combining our independent modifications we arrive at a maximum improvement of a factor of roughly 10, meaning that the majority of the initial discrepancy remains unexplained. We propose three possible outcomes. There exist other physically justifiable modifications of the basic space charge model that aligns the model with experimental data; one or several of the assumptions in our impedance calculations from the basic space charge model are inaccurate or not correct and the present results are hence not valid; or the basic space charge model does not accurately describe GB impedance at the level of individual GBs.

6. Methodology

The BZY15 sample was commercially produced by NORECS (Norway), sintered with the SSRS method with 1 wt% NiO. The sample diameter was 20 mm, with an electrode diameter of 10 mm and a sample thickness 1.0 mm. For the impedance spectroscopy measurements we applied a frequency range 0.1 Hz to 5 MHz in wet inert atmosphere, using a ProboStat sample holder cell produced by NORECS.

The DFT calculations were performed with the VASP code [40,41], employing the generalized gradient approximation (GGA-PBE) [42] and projected augmented wave method (PAW) [43] potentials. The calculations on the (210)[001] GB supercell, with dimensions $\sqrt{5}a_0 \times 2a_0 \times 4\sqrt{5}a_0$, were performed in two steps. First, a defect free GB supercell was relaxed with no volume constraints. Second, protons were introduced to the relaxed supercell, and the energy was minimized under constant volume conditions. The plane wave cut-off energy was 600 eV for volume relaxations and 470 eV for constant volume calculations, and the ionic relaxations was considered to be converged when the residual forces were smaller than 0.03 eV $Å^{-1}$. For the proton calculations, a homogeneous background charge with opposite sign was added to retain charge neutrality. We applied *k*-point densities of $3 \times 3 \times 1$ according to the Monkhorst-Pack scheme. To find the cluster binding energy, ΔE_t, a bulk $(5 \times 5 \times 5)$ cubic supercell was used with defects far apart in the same cell, with a gamma centered *k*-point density of $1 \times 1 \times 1$.

CRediT authorship contribution statement

Tarjei Bondevik: Conceptualization, Methodology, Software, Formal analysis, Investigation, Writing - original draft, Visualization. **Jonathan M. Polfus:** Conceptualization, Methodology, Resources, Writing - review & editing. **Truls Norby:** Conceptualization, Methodology, Resources, Writing - review & editing, Supervision, Project administration.

Declaration of competing interest

We have no conflict of interest to declare.

Acknowledgement

The authors would like to thank Dr. Rotraut Merkle and Prof. Joachim Maier at MPI, Stuttgart, for fruitful discussions. Financial support from the Research Council of Norway, project Nano2021/228355 “Functional oxides for clean energy technologies: fuel cells, gas separation membranes and electrolysers” (FOXCET) conducted by SINTEF Industry, University of Oslo, and NTNU, is gratefully acknowledged.

Appendix A. Supplementary data

Supplementary data to this article can be found online at https://doi.org/10.1016/j.ssi.2020.115369.

References

[1] C. Kjølseth, et al., Space–charge theory applied to the grain boundary impedance of proton conducting $BaZr_{0.9}Y_{0.1}O_3$, Solid State Ionics 181 (2010) 268–275.
[2] C.-T. Chen, C.E. Danel, S. Kim, On the origin of the blocking effect of grain-boundaries on proton transport in yttrium-doped barium zirconates, J. Mater. Chem. 21 (2011) 5435–5442.
[3] F. Iguchi, et al., Direct evidence of potential barriers at grain boundaries in Y-doped $BaZrO_3$ from dc-bias dependence measurements, J. Mater. Chem. 21 (2011) 16517–16523.
[4] M. Shirpour, R. Merkle, J. Maier, Space charge depletion in grain boundaries of $BaZrO_3$ proton conductors, Solid State Ionics 225 (2012) 304–307.
[5] M. Shirpour, et al., Dopant segregation and space charge effects in proton-conducting $BaZrO_3$ perovskites, J. Phys. Chem. 116 (2012) 2453–2461.
[6] M. Shirpour, R. Merkle, J. Maier, Evidence for space charge effects in Y-doped $BaZrO_3$ from reduction experiments, Solid State Ionics 216 (2012) 1–5.
[7] M. Shirpour, et al., Nonlinear electrical grain boundary properties in proton conducting Y–$BaZrO_3$ supporting the space charge depletion model, Phys. Chem. Chem. Phys. 14 (2012) 730–740.
[8] A. Lindman, E.E. Helgee, G. Wahnström, Comparison of space-charge formation at grain boundaries in proton-conducting $BaZrO_3$ and $BaCeO_3$, Chem. Mater. 29 (18) (2017) 7931–7941.
[9] J.M. Polfus, M. Pishahang, R. Bredesen, Influence of Ce^{3+} polarons on grain boundary space-charge in proton conducting Y-doped $BaCeO_3$, Phys. Chem. Chem. Phys. 20 (2018) 16209–16215.
[10] H. Fjeld, et al., Charge carriers in grain boundaries of 0.5% Sr-doped $LaNbO_4$, Solid State Ionics 181 (3) (2010) 104–109.
[11] R.A.D. Souza, The formation of equilibrium space-charge zones at grain boundaries in the perovskite oxide $SrTiO_3$, Phys. Chem. Chem. Phys. 11 (2009) 9939–9969.
[12] X. Guo, J. Maier, Grain boundary blocking effect in zirconia: a Schottky barrier analysis, J. Electrochem. Soc. 148 (2001) 121–126.
[13] X. Guo, R. Wasser, Electrical properties of the grain boundaries of oxygen ion conductors: acceptor-doped zirconia and ceria, Prog. Mater. Sci. 51 (2006) 151–210.
[14] A. Tschöpe, E. Sommer, R. Birringer, Grain size-dependent electrical conductivity of polycrystalline cerium oxide: I. Experiments, Solid State Ionics 139 (3) (2001) 255–265.
[15] A. Tschöpe, S. Kilassonia, R. Birringer, The grain boundary effect in heavily doped cerium oxide, Solid State Ionics 173 (1) (2004) 57–61.
[16] J.-S. Kim, et al., Proton conduction at BaO-terminated (001) $BaZrO_3$ surface using density functional theory, Solid State Ionics 275 (2015) 19–22.
[17] J.M. Polfus, J. Yang, B. Yildiz, Interplay between H_2O and CO_2 coadsorption and space-charge on Y-doped $BaZrO_3$ surfaces, J. Mater. Chem. A 6 (2018) 24823–24830.
[18] J.M. Polfus, T. Norby, R. Bredesen, Proton segregation and space-charge at the $BaZrO_3$ (0 0 1)/MgO (0 0 1) heterointerface, Solid State Ionics 297 (2016) 77–81.
[19] S. Kim, J. Fleig, J. Maier, Space charge conduction: simple analytical solutions for ionic and mixed conductors and application to nanocrystalline ceria, Phys. Chem.

Chem. Phys. 5 (2003) 2268–2273.
[20] R.A.D. Souza, et al., Defect chemistry of grain boundaries in proton-conducting solid oxides, Solid State Ionics 196 (1) (2011) 1–8.
[21] P.C. McIntyre, Equilibrium point defect and electronic carrier distributions near interfaces in acceptor-doped strontium titanate, J. Am. Ceram. Soc. 83 (5) (2000) 1129–1136.
[22] A. Tschöpe, Grain size-dependent electrical conductivity of polycrystalline cerium oxide II: space charge model, Solid State Ionics 139 (3) (2001) 267–280.
[23] J. Polfus, et al., Defect chemistry of a $BaZrO_3$ Σ3 (111) grain boundary by first principle calculations and space-charge theory, Phys. Chem. Chem. Phys. 14 (2012) 12339–12346.
[24] E.E. Helgee, A. Lindman, G. Wahnström, Origin of space charge in grain boundaries of proton-conducting eBaZrO3, Fuel Cells 13 (2013) 19–28.
[25] A. Lindman, E. Helgee, G. Wahnström, Theoretical modeling of defect segregation and space-charge formation in the $BaZrO_3$ (210)[001] tilt grain boundary, Solid State Ionics 252 (2013) 121–125.
[26] J.-H. Yang, B.-K. Kim, Y.-C. Kim, Calculation of proton conductivity at the Σ3(111)/[110] tilt grain boundary of barium zirconate using density functional theory, Solid State Ionics 279 (C) (2015) 60–65.
[27] J.-H. Yang, et al., High activation energy for proton migration at Σ3(111)/[110] tilt grain boundary in barium zirconate, Solid State Ionics 252 (2013) 126–131.
[28] K.D. Kreuer, Proton-conduction oxides, Annu. Rev. Mater. Res. 33 (2003) 333–359.
[29] J. Fleig, S. Rodewald, J. Maier, Microcontact impedance measurements of individual highly resistive grain boundaries: general aspects and application to acceptor-doped $SrTiO_3$, J. Appl. Phys. 87 (2000) 2372–2381.
[30] L. Young, Anodic oxide films. Part 4. The interpretation of impedance measurements on oxide coated electrodes on niobium, Trans. Faraday Soc. 51 (1955) 1250–1260.
[31] S.M. Haile, The role of microstructure and processing on the proton conducting properties of gadolinium-doped barium cerate, J. Mater. Res. 13 (1998) 1576–1595.
[32] Y. Yamazaki, et al., Proton trapping in yttrium-doped barium zirconate, Nat. Mater. 12 (2013) 647–651.
[33] E. Jones, et al., SciPy: Open Source Scientific Tools for Python, (2001).
[34] F. Iguchi, N. Sata, H. Yugami, Proton transport properties at the grain boundary of barium zirconate based proton conductors for intermediate temperature operating SOFC, J. Mater. Chem. 20 (2010) 6265–6270.
[35] D.S. Mebane, R.A. De Souza, A generalised space-charge theory for extended defects in oxygen-ion conducting electrolytes: from dilute to concentrated solid solutions, Energy Environ. Sci. 8 (2015) 2935–2940.
[36] X. Tong, D.S. Mebane, R.A. De Souza, Analysing the grain-boundary resistance of oxide-ion conducting electrolytes: Poisson-Cahn vs Poisson-Boltzmann theories, J. Am. Ceram. Soc. 103 (2019) 5–22.
[37] J. Fleig, et al., Inhomogeneous current distributions at grain boundaries and electrodes and their impact on the impedance, Solid State Ionics 113-115 (1998) 739–747.
[38] J. Fleig, J. Maier, The impedance of ceramics with highly resistive grain boundaries: validity and limits of the brick layer model, J. Eur. Ceram. Soc. 19 (6) (1999) 693–696.
[39] J. Fleig, The influence of non-ideal microstructures on the analysis of grain boundary impedances, Solid State Ionics 131 (1) (2000) 117–127.
[40] G. Kresse, J. Hafner, Ab initio molecular dynamics for liquid metals, Phys. Rev. B 47 (1993) 558–561.
[41] G. Kresse, J. Furthmüller, Efficient iterative schemes for ab initio total-energy calculations using a plane-wave basis set, Phys. Rev. B 54 (1996) 11169–11186.
[42] J.P. Perdew, K. Burke, M. Ernzerhof, Generalized gradient approximation made simple, Phys. Rev. Lett. 77 (1996) 3865–3868.
[43] G. Kresse, D. Joubert, From ultrasoft pseudopotentials to the projector augmented-wave method, Phys. Rev. B 59 (1999) 1758–1775.